

# The consistency of interdecadal changes in the Earth's rotation variations

Yachong An, Hao Ding\*, Zhifeng Chen

*Department of Geophysics, School of Geodesy and Geomatics, Key Laboratory of Geospace Environment and Geodesy of the Ministry of Education, Wuhan University, 430079, Wuhan, China*

\*Corresponding address: [dhaosgg@sgg.whu.edu.cn](mailto:dhaosgg@sgg.whu.edu.cn)

## Key points

1. For the first time, we restored the waveforms of the  $\sim 5.9\text{yr}/\sim 8.5\text{yr}$  signals from the PM and confirm that they have time-varying amplitudes.
2. We find that the  $\sim 5.9\text{yr}$  oscillations (SYOs) (and the  $\sim 8.5\text{yr}$  oscillations (EYOs)) in the  $\Delta\text{LOD}$  and the PM have good consistency.
3. The new findings demonstrate that the SYOs/EYOs in the  $\Delta\text{LOD}$  and in the PM may come from the same source in Earth's interior (perhaps core motions).

## Abstract

To accurately restore interdecadal oscillations from the length of day variation ( $\Delta\text{LOD}$ ) and the polar motion (PM), we propose a normal time-frequency transform (NTFT) combining with curve fitting scheme. Compared with the NTFT, the combined NTFT with a boundary extreme point mirror-image-symmetric extension (BEPME) process, and singular spectrum analysis (SSA) in some simulated tests, the superiority and reliability of this new scheme have been confirmed; and we further verified the validity of it in a mature case analysis from the Earth's free oscillation modes  ${}_0\text{S}_0$  and  ${}_1\text{S}_0$ . After then, we use it to restore the  $\sim 5.9\text{yr}$  oscillation (referred to as SYO) and  $\sim 8.5\text{yr}$  oscillation (referred to as

EYO) from the  $\Delta$ LOD and the PM records. Our results reconfirm that the SYO and EYO in the  $\Delta$ LOD (and PM) have no stable damping trend (which is different from results in some previous studies), and for the first time, we find that the SYOs (and EYOs) contained in the  $\Delta$ LOD and the PM show very good consistency. Such consistency demonstrates that the SYOs/EYOs in the  $\Delta$ LOD and the PM must come from the same source. As the external excitation sources of the Earth rotation contain no such oscillations, we suggest that core motions are possible sources.

### **Plain Language Summary**

The interdecadal variations in the Earth's rotation are generally considered that should come from Earth's interior, but their physical mechanisms are still not well established due to limited observational information. There is a debate about whether the SYO/EYO in the  $\Delta$ LOD has stable damping trend (e.g., Holme & de Viron, 2013; Duan et al., 2018; Ding, 2019; Duan & Huang, 2020; Ding, et al., 2021), and there is no study has given clearly evidence to show the robust relationships between the SYO/EYO in the  $\Delta$ LOD and in the PM (except for the close periods). Hence, any additional correlation could contribute to deeper geophysical insights about SYO/EYO in the Earth system. Here, we use longer data records to focus on how the SYOs/EYOs change in the  $\Delta$ LOD and in the PM. We find that the SYOs in the  $\Delta$ LOD and in the  $m_2$  component of the PM have almost oppose phases, and the EYOs in the  $\Delta$ LOD and the  $m_1$  component of the PM have almost same phases. Such good consistency provides strong constraint for building core-mantle coupling model based on the geomagnetic observations.

## **1. Introduction**

As a dynamic system, the Earth is affected by some internal dynamic processes, external mass transport and the gravitational attraction of the Sun, Moon and planets; hence, the Earth's rotation is changing (Gross, 1993, 2015). The instantaneous position of the Earth's rotation vector is described by the three components ( $m_1$ ,  $m_2$ ,  $m_3$ ), where  $m_1$  and  $m_2$  describe polar motion (PM) ( $m_1+im_2$ ), and  $m_3$  describes variations in the rotation rate (directly proportional to changes in the length of day (LOD)) (Wahr, 1985). The decadal variations in the Earth's rotation have been studied since the 1960s, but the cause of those variations is currently unknown (see Gross (2015) for a review). Recently, two interdecadal periodic signals, an  $\sim$ 5.9yr oscillation (referred to as SYO) and an  $\sim$ 8.5yr oscillation (referred to as EYO), have been identified in the Earth's rotation variations. The SYO was first found in the LOD variation ( $\Delta$ LOD) in the 1990s, followed by many studies of its complex frequency and possible excitations (e.g., Holme and de Viron, 2013; Ding, 2019; Chen et al., 2019; Ding et al., 2021). However, no undoubtedly physical mechanism or excitations have been drawn for it (see Ding et al. (2021) for a review). Recently, Ding et al. (2019) and Chen et al. (2019) have found the SYO in the PM independently. Although Bizouard (2018) has denoted that the amplitude modulation of between the Chandler wobble and the Annual wobble in the 1890-2017 PM time series have a  $\sim$ 6.4yr period, it is different from the periodic SYO in the PM which was found by Ding et al. (2019) and Chen et al. (2019). Both of Ding et al. (2019) and Chen et al. (2019) confirmed that the Earth's external sources (i.e., atmospheric, oceanic, and hydrological effects) cannot be explained as the sources of this SYO signal in the PM. Chen et al. (2019) concluded that such a finding helps to further understand the physical mechanism of the SYO in the Earth's rotation variations, and they suggested that the SYO should come from some core motions. The EYO was first identified from the  $\Delta$ LOD in Ding (2019), and subsequently, Ding et al. (2019) also found it in the PM. After confirming that

atmospheric/oceanic/hydrological effects cannot excite this signal, Ding et al. (2019) suggested it might be the possible inner core wobble (ICW).

The SYO has been found to have good consistency in the  $\Delta$ LOD, the GPS and geomagnetic records (Ding and Chao, 2018a). Chen et al. (2019) investigated the excitations of the SYO in all three components of Earth rotation upon using sinusoidal fit, but no consistency was found. Zotov (2019) compared the SYO in the  $\Delta$ LOD and the amplitude envelopes of the Chandler and Annual wobbles in the PM, their results clearly shown that the latter has different period (~6.4yr; which is same as the one suggested by Bizouard (2018)) with the SYO in the  $\Delta$ LOD (see P35 of Zotov (2019)). Besides, the amplitude envelopes of the Chandler and Annual Wobbles in the PM does not mean that there must be a ~6.4yr signal in the PM, this can be easily confirmed by a test. So far, except for the almost same periods, no study has found that the SYO (and the EYO) in the  $\Delta$ LOD and PM have clear relations. As Sir Newton has said, *therefore to the same natural effects we must, as far as possible, assign the same causes.* If we can find any possible relationship between the ~5.9yr (and the ~8.5yr) signals contained in the  $\Delta$ LOD and PM, it will help us to find the *same* cause of them. Based on the data observed by astronomical observations and derived from existing climate models, we mainly focus on this purpose in this study.

For our purposes, we propose a curve fitting scheme to improving the frequency resolutions of the NTFT in section 2.2. In section 3.1, we compare the restored results of several different methods to confirm the superiority and reliability of this new scheme. To further verify the validity of this new scheme, we extract Earth's free oscillation modes after the 2011 Mw9.1 Tohoku earthquake, and compare our results with those of previous studies in section 3.2. Finally, we use it to restore the SYOs/EYOs in the  $\Delta$ LOD and PM and investigate whether they have some relationships in section 4.

## 2 Data and Method

### 2.1 Datasets

A yearly long-term  $\Delta$ LOD record (1860/06-2019/06) (Stephenson and Morrison, 1985) was chosen, the 1962-2019 part of which was obtained from the EOPC04  $\Delta$ LOD record (Bizouard et al., 2019), and the 1860-1900 part of it has an  $\sim$ 0.18ms precision, which is too large, so we only use this part to improve the frequency resolution (i.e., we tend to trust only the results obtained in the 1900-2019 timespan). The 1861/01-2019/12 EOPC01 time series with 0.1-year sampling was chosen for the PM ( $m_1$  and  $m_2$ ; the  $m_1$  component along the Greenwich meridian and the  $m_2$  component along 90°E longitude) record. For the same reason as above, we only trust the results obtained in the 1900-2019 timespan.

For the three external excitation sources of the  $\Delta$ LOD and PM, i.e., the atmospheric, oceanic, and hydrological effects, we downloaded the atmospheric angular momentum (AAM) record and oceanic angular momentum (OAM) record from the Special Bureau for the Atmosphere and the Special Bureau for the Oceans, respectively. Chen et al. (2019) have estimated the hydrological effects for the SYO in the PM and  $\Delta$ LOD in the excitation domain, the corresponding values are not very significant (even less than the background noise level), especially the hydrological effect for the SYO in the  $\Delta$ LOD, which is only 0.001ms (too little, so that can be ignored). Given that Ding (2019), Chen et al. (2019) and Ding et al. (2019) confirmed that the hydrological effects have no significant contribution in the target 5.5-10yr period band and that different hydrological models have clear deviations (Ding et al., 2019), we do not further consider hydrological effects. Both of the AAM and OAM records were preprocessed and resampled (1yr sampling for the  $\Delta$ LOD and 0.1yr for the PM), and the final AAM

and OAM records used had a common 1949/06-2019/06 timespan. More details about the preprocessing for the  $\Delta\text{LOD}$ , PM, AAM and OAM used can be found in Ding (2019) and Ding et al. (2019). The AAM and OAM excited PM and  $\Delta\text{LOD}$  were further calculated for use (Munk and MacDonald, 1960; Barnes et al., 1983; Eubanks, 1993). The  $\Delta\text{LOD}/\text{PM}$  time series, the AAM/OAM excited  $\Delta\text{LOD}/\text{PM}$  time series, and their corresponding Fourier spectra are shown in Figs. 1 and 2.

From Fig. 1b, we can find that the effects of AAM+OAM are below the background noise level of the used  $\Delta\text{LOD}$  in the target band (5.5-10yr) (see the gray area), and there is no spectral peak in the AAM+OAM corresponds to the target SYO and EYO. Hence, we further confirm that the AAM and OAM have no visible effects on the SYO and EYO. But there is significant spectral peak around  $\sim 5\text{yr}$  (0.2cpy) in the spectra of the AAM+OAM (which is mainly came from AAM), which will affect the identification of the SYO (similar to the findings in previous studies (Chen et al., 2019)). Hence, the AAM effects must be removed when we try to restore the SYOs from the Earth's rotation variations, but this process is not needed for the EYOs. Fig. 2 also confirms that the AAM+OAM have no significant contribution for the target SYO and EYO in the PM (also same as the findings in Chen et al. (2019)).

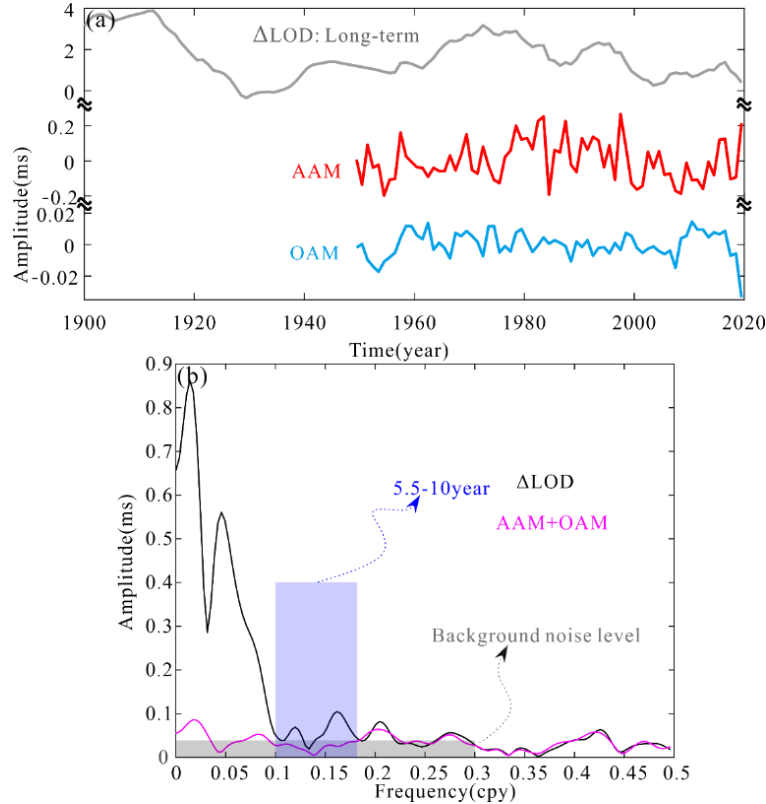


**Figure 1.** (a) The 1900-2020 part of the used 1861-2020  $\Delta\text{LOD}$  record, and the excited  $\Delta\text{LOD}$  by the AAM/OAM; (b) The Fourier spectra of the observed  $\Delta\text{LOD}$  and the AAM+OAM excited  $\Delta\text{LOD}$  for the same 1949-2020 time span. The gray area denotes the background noise level of the observed  $\Delta\text{LOD}$  in the 0-0.3cpy frequency band; the blue area denotes the target frequency band.

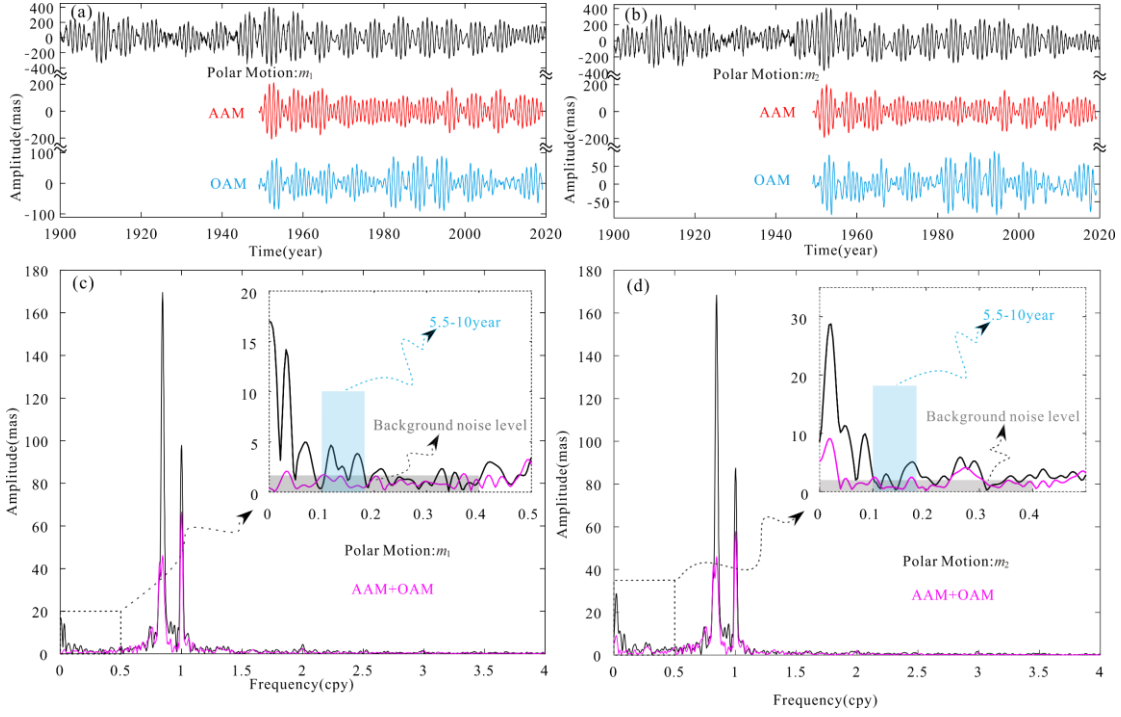


**Figure 2.** (a) The  $m_1$  component of observed PM (1900-2020), excited PM by AAM (red curve) and OAM (blue curve); (c) The Fourier spectra of the time series shown in (a) (for the 1949-2020 time-span). (b) and (d) similar to (a) and (c), but for the  $m_2$  component. The subplots are zooms correspond to the 0-0.5 cpy band in main panel (c) and (d), the gray area denotes the background noise level of the observed PM in the 0-0.4 cpy, and the blue area denotes the band of 5.5-10yr period.

Hence, in the following, we mainly use two types of datasets: 1) The residual  $\Delta\text{LOD}$  and PM ( $m_1$  and  $m_2$ ) time series (from 1949-2019), in which the AAM and OAM effects have been removed. These residual time series are used for the SYO; 2) The original 1860/06-2019/06 yearly  $\Delta\text{LOD}$  record and the original 1861/01-2019/12 yearly EOPC01 PM time series. These time series are used for the EYO.

## 2.2 Improving the frequency resolution of NTFT

In this study, we mainly use the normal time-frequency transform (NTFT), which was proposed by Liu et al. (2007) and Liu and Hsu (2009, 2011). This method can identify and extract the

instantaneous information of harmonics/quasi-harmonics signals as a filter (Liu et al., 2007; Cai et al., 2018). The NTFT method has been proven to have high robustness and has been used in different studies (Liu et al., 2007; Su et al., 2014; Cai et al., 2018; Duan and Huang, 2019; Cui et al., 2020). However, when the length of the available record is limited, the NTFT has insufficient frequency resolution for relatively low-frequency signals. To overcome this, a boundary extreme point mirror-image-symmetric extension (BEPME) process has been proposed (Duan et al. 2015), and Duan and Huang (2020) have used the NTFT+BEPME process to restore the SYO and the EYO from the  $\Delta$ LOD. However, Ding et al. (2021) have shown that such a process produces some strange results: even for a stable cosine signal, the restored result from the NTFT+BEPME process has a stable damping trend. Here, we develop a different scheme by virtue of curve iteration fitting, and we give a simple introduction to it. Here we firstly give a simple introduction to NTFT, and we recommend that readers refer to Liu et al. (2007) and Liu and Hsu (2009, 2011) for more details.

For the time function  $f(t) \in C$  ( $C$  is the complex field), its time-frequency transform can be written as (Liu and Hsu, 2009; Su et al., 2014)

$$\Psi f(\tau, \varpi) = \int_{-\infty}^{+\infty} f(t) \overline{\psi(t - \tau, \varpi)} dt, \quad \tau, \varpi \in R \quad (1)$$

where  $\tau$  and  $\varpi$  is the local time and frequency, respectively. ‘ $\bar{-}$ ’ denotes complex conjugation,  $\psi(t, \varpi)$  denotes the kernel function, and  $R$  represents the real field. A typical NTFT kernel can be written as (e.g., Liu and Hsu, 2009; Su et al., 2014; Cai et al., 2018; Cui et al., 2020)

$$\psi(t, \varpi) = |\mu(\varpi)| w(\mu(\varpi)t) \exp(i\varpi t), \quad \mu(\varpi) \in R \quad (2)$$

where the real function  $\mu(\varpi)$ , called the time-frequency resolution adaptor, determines the type of NTFT. The function  $w(t)$  is a normal window, which is generally used as a normal Gaussian window (e.g., Liu and Hsu, 2009), written as

$$w(t) = \frac{1}{\sqrt{2\pi}\sigma} \exp\left(-\frac{t^2}{2\sigma^2}\right) \quad (3)$$

where  $\sigma > 0$  denotes the window width parameter. For a complicated time series which contains many different harmonics, assume that average angular frequency of the target signal is  $\omega_1$ , and the interference signal has a  $\omega_2$  frequency, which is the one closest to  $\omega_1$ ; then,  $\sigma$  should satisfy

$$\sigma \geq \left| \frac{\mu(\omega_1)}{\omega_2 - \omega_1} \right| \sqrt{-2 \ln(\eta)} \quad (4)$$

where  $\eta$  indicates the percentage of the residual interference signal in the extracted result to the original interference signal (higher accuracy requires a smaller  $\eta$  value, and Liu and Hsu (2009) suggested taking  $\eta$  as 1%). For a given  $\omega_1$ , a closer  $\omega_2$  means that we need a much longer length for the used time series (i.e., wider window). The frequency resolution of the NTFT depends on the actual length of the window  $w(t)$ , which is directly associated with both the time-frequency resolution adaptor  $\mu(\varpi)$  and the window width parameter  $\sigma$  (a higher  $\sigma$  value corresponds to a wider  $w(t)$ ). Similar to other linear time-frequency transforms, the NTFT has to obey Heisenberg's uncertainty principle (Cohen, 1989, 1995). Although a larger  $\sigma$  means a higher frequency resolution, the frequency resolution cannot be improved arbitrarily because the length of the used time series limits the effective length of the window. In addition, the function  $R_g(\varpi)$  allows measurement of the range of the edge effect (95% confidence intervals)

$$R_g(\varpi) = \frac{1.643\sigma}{|\mu(\varpi)|} \quad (5)$$

Hence, the edge effect ranges increase with the length of the window.

According to the discussion above, if we can identify the closer signals and then fit and remove them,  $\sigma$  will be smaller. Hence, we can first detect the possible periodic signals in the used record, and then fit and remove the closer signals (to the target signal) upon using an interactive least square

process. This fitting and removing process is similar to that used in Holme and de Viron (2013) and Ding (2019), in which they have confirmed that such a process does not change the original target periodic signals. After removing all the related interference, we can finally filter the processed record adopting the NTFT with a small value of  $\sigma/|\mu(\varpi)|$ . Note that this NTFT+curve fitting process also produces an edge effect due to the NTFT and the error in the detected frequency, but it is trivial because of a small value of  $\sigma/|\mu(\varpi)|$ . In the following, we first verify this new proposed process.

### 3 Verifications of the NTFT+curve fitting process

#### 3.1 Verification from simulated data

Here, eleven *cosine* periodic signals (5.9yr, 7.6yr, 8.5yr, 11yr, 13.5yr, 15.6yr, 18.6yr, 22.3yr, 33yr, 68yr, and 149yr) and rand noise (has a 0.015ms mean amplitude in the frequency domain) are used to synthesize the real observed EOPC04  $\Delta$ LOD time series ( $\Delta$ LOD-AAM-OAM), all of those 11 signals have been identified from the  $\Delta$ LOD by previous studies (Ding, 2019; Ding et al., 2021). The simulated time series  $g_1(t)$  (from 1962-2020) and the observed residual EOPC04  $\Delta$ LOD time series are shown in Fig. 3a (both of them have a one month sampling interval). Their corresponding Fourier spectra (gray curve and red curve) are shown in Fig. 3b; we can see that the spectra of the simulated time series are almost completely overlapped with those of the real  $\Delta$ LOD time series, which means that those 11 signals can well represent the low-frequency terms of the real observed  $\Delta$ LOD. Besides, to test overfitting, we also further the Fourier spectra of a simulated time series  $g_2(t)$  which only contains the 5.9yr, 7.6yr, 8.5yr signals (see the dashed blue curve in Fig. 3b). Considering the Fourier spectral leakage from the low-frequency terms (less than 0.1cpy), we can say that those three simulated cosine signals still can well represent the corresponding spectral peaks of the real observed  $\Delta$ LOD. This finding

further demonstrates that there is no over-fitting phenomenon when we use the 11 periodic cosine signals to fit the real observed  $\Delta\text{LOD}$ . In addition, we only identify very little information ( $\sim 5.9\text{yr}$ ,  $\sim 8.6\text{yr}$  and some overlapping low frequency signals) from the Fourier spectra of the simulated time series (Fig. 3b) due to the low frequency resolution. To apply the NTFT+curve fitting, we firstly detect weak harmonic signals in the simulated time series using the stabilized AR-z spectral method (Ding and Chao, 2018b), which has the higher frequency resolutions. The AR-z spectra of  $g_1(t)$  is shown in Fig. 3c; we can clearly identify the 4 input signals (5.9yr, 7.6yr, 8.5yr and 11yr) from the AR-z spectra in the 0.075-0.5cpy band.

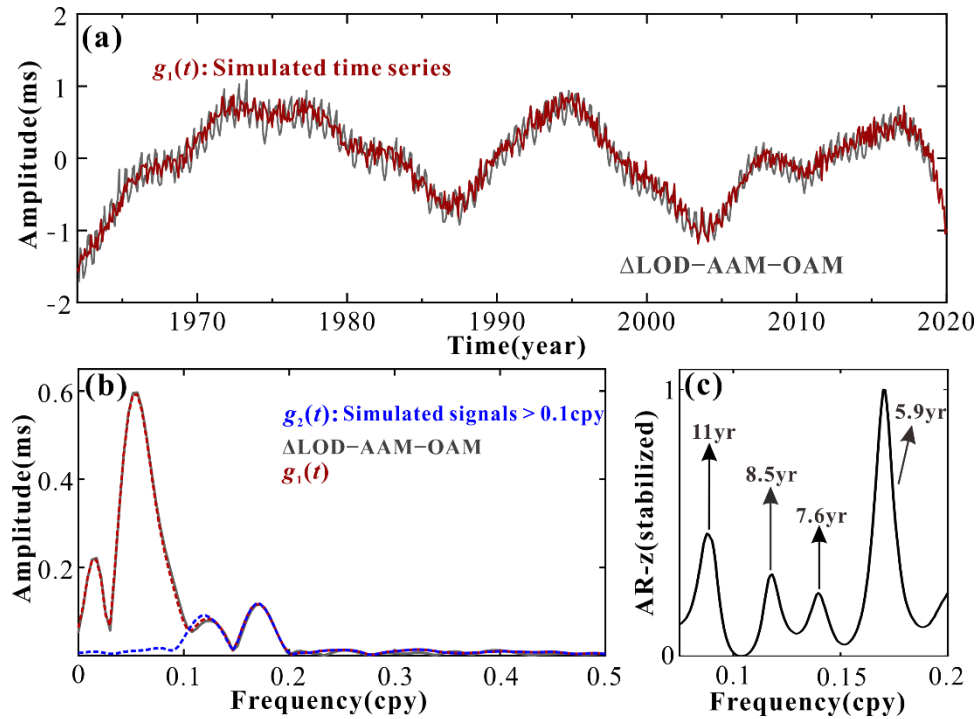


**Figure 3.** (a) The residual EOPC04  $\Delta\text{LOD}$  (1962-2020) with one-month sampling (gray curve) and the simulated time series (red curve). (b) The Fourier spectra of the residual EOPC04  $\Delta\text{LOD}$  (gray curve), the simulated time series which contain 11 cosine signals, and the simulated time series which only contain the 5.9yr, 7.6yr and 8.5yr signals (blue curve). (c) The stabilized AR-z spectra of the simulated time series  $g_1(t)$  in the 0.075-0.5cpy band.

To verify the validity and superiority of our scheme, we individually use the NTFT, NTFT+BEPME, and NTFT+curve fitting processes (using the above detected frequency) to restore the input SYO and EYO from the simulated time series. Given that singular spectrum analysis (SSA) has been maturely used to extract trends and periodic oscillations from time series (Vautard et al., 1992; Walwer et al., 2016; Modiri et al., 2020), we also show the restored results from SSA. The obtained results for SYO and EYO are shown in Figs. 4a and 4b, respectively. Compared with the input SYO/EYO (black curve in Fig.4a/4b), the restored SYO/EYO from the NTFT+curve fitting process is the closest one (although it also has slight end deviations), while the restored SYO/EYO from NTFT has time varying amplitudes, and the restored SYO/EYO from SSA has the most serious deviation from the input SYO/EYO. Although we adopt the real boundary extreme points to get the most ideal effect (In fact, the yellow curves in Figs. 4a and 4b show that the boundary extreme points obtained upon using the NTFT as described in Duan et al. (2015) are always biased), the restored SYO/EYO from NTFT+BEPME has damping amplitudes (similar to those shown in Ding et al. (2021)). This test demonstrates the validity and superiority of our scheme. We also show other simulated tests in the SI, all of which show similar results as those obtained here (see Supplementary Figs. S1-S2). Besides, in the Figures S3-S4 of the SI, we further explain why the NTFT+BEPME process yields a strange (e.g., stable decaying or increased) waveform.

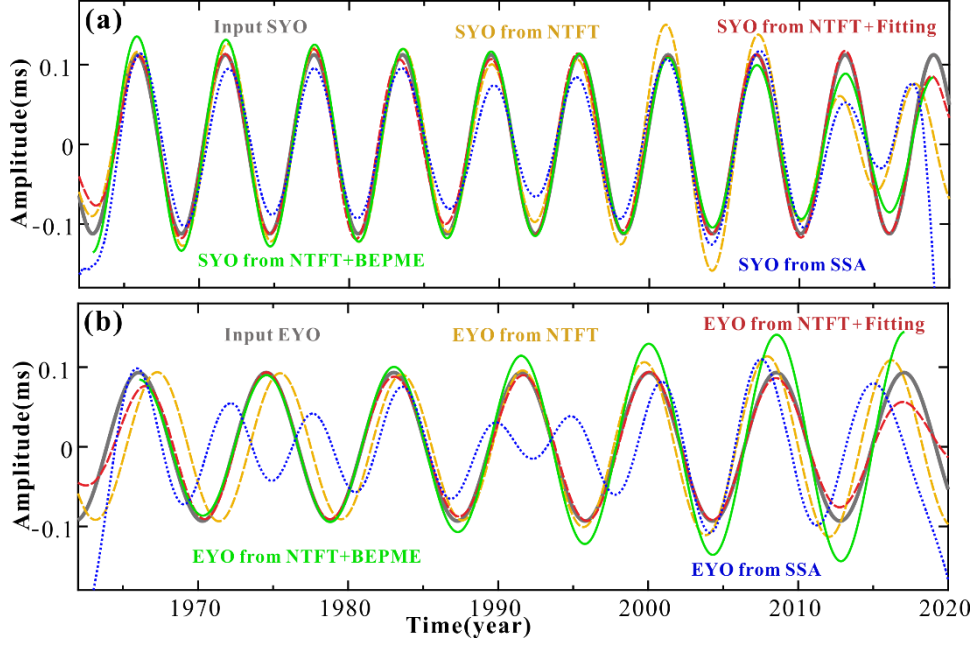


**Figure 4.** (a) The input stable cosine 5.9yr signal (SYO; gray curve) and the restored results by using the NTFT (dashed yellow curve), NTFT+BEPME (green curve), NTFT+curve fitting processes (dashed red curve) and SSA (dotted blue curve). (b) Similar to (a) but for the EYO.

After the above verification, we will further test the robustness of the above used different methods. In this test, we replace the 5.9yr signal in the above simulated test to two different signals, a 5.6yr signal and a 6.4yr signal; the other 10 cosine signals are same as those in the above simulated time series. Figure 5a shows the real observed  $\Delta\text{LOD}$  and the simulated time series, their corresponding Fourier spectra (gray curve and red curve) are shown in Fig. 5b. Figure 5b also shows that there is only a significant spectral peak in the same frequency bin (5.9yr frequency) in observation and simulation. This also indicates that the Fourier transform cannot distinguish two closed signals (5.5yr and 6.4yr) due to the limited frequency resolution. Pretend we don't know whether it corresponds to a single periodic signal or not, we 'blindly' use above mentioned methods to restore signal around the 0.1695cpy frequency bin (i.e., the frequency of the 5.9yr signal). But for the

NTFT+curve fitting processes, we firstly detect weak signals from the simulated time series using the stabilized AR-z spectra as shown in Fig. 5c; all added signals (5.6yr, 6.4yr, 7.6yr, 8.5yr and 11yr) are recognized. Based on those detected results from the AR-z spectrum, we use the NTFT+curve fitting processes to restore signal around the 0.1695cpy frequency bin. The obtained results are shown in Fig. 5d. When the SYO is not added to the simulated time series, comparing with the restored results from other methods, the restored result of NTFT+ curve fitting has the smallest amplitude (close to the amplitude of added rand noise). Meanwhile, the restored result from NTFT+ BEPME still has damping amplitude. Besides, the restored SYO results of the NTFT and SSA also have large amplitudes, although SYO is not add to the simulated time series. This test demonstrates the robustness of our scheme, i.e., our scheme can avoid to restore ‘wrong’ signal.

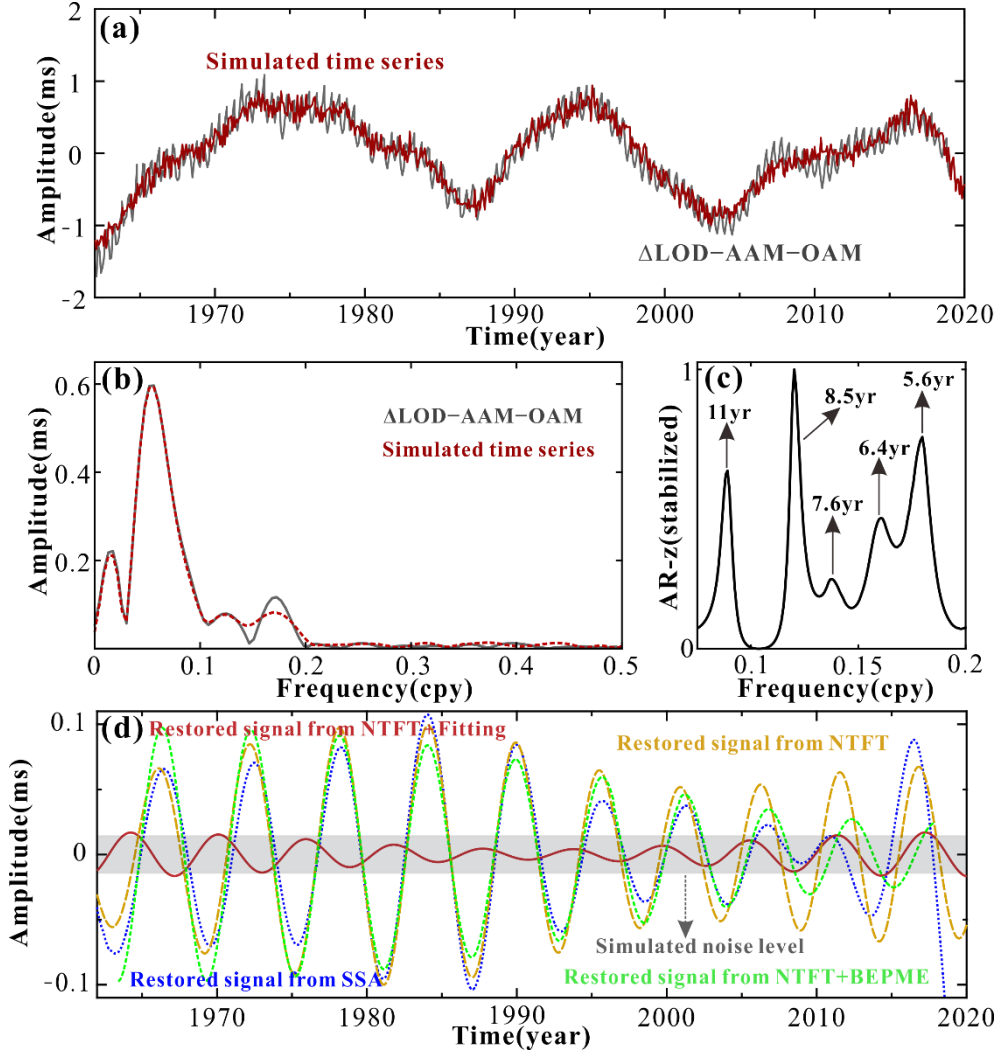


**Figure 5.** (a) The residual EOPC04  $\Delta\text{LOD}$  (1962-2019) with one-month sampling (gray curve) and the simulated time series (red curve). (b) The Fourier spectra of the real observed  $\Delta\text{LOD}$  time series and simulated time series shown in (a). (c) The stabilized AR-z spectra of the simulated time series in the 0.075-0.5cpy band. (d) The restored results by using the NTFT (yellow curve), NTFT+BEPME (green curve), NTFT+curve fitting processes (red curve) and SSA (blue curve) near the SYO band; The gray area denotes the amplitude of added rand noise (0.015ms).

### 3.2 Verification from well-determined normal mode signals

In addition to Liu et al. (2007) using NTFT to restore the Chandler wobble from the PM, NTFT

has also been used to restore the normal modes of the Earth's free oscillations (e.g., Duan and Huang, 2019). Unlike the Chandler wobble, which has uncertain time-varying amplitudes in the time domain (Gross, 2015), the normal modes of the Earth's free oscillations are stable *cosine* oscillations with fixed attenuations. Hence, here, we use the NTFT+curve fitting process to restore the  ${}_0S_0$  mode as an example and compare the obtained results with those of previous studies.

We choose 14 superconducting gravimeter (SG) records (with one minute sampling) after the 2011 Mw9.1 Tohoku earthquake as the datasets. All of these records began 1 hour after the event and were 500 hours length. The solid/ocean tides and atmospheric effects are removed (details of these 14 records can be found in Supplementary Figs. S5-S6). We use the NTFT+curve fitting process to those 14 records one by one, and then the waveforms for  ${}_0S_0$  in the time domain are obtained (see Supplementary Fig. S5a in the SI for some examples); hence, we can obtain the frequency of  ${}_0S_0$  for each record from their corresponding time-varying observation frequency (Fig. S6a in the SI), and its  $Q$  value can be calculated by fitting the amplitude envelope from the time domain using the least square process (see Fig. S6a in the SI). We finally use the weighted value of those 14 different estimated complex frequencies as the recommended values (see the green lines in Figs. 6b and 6c). The PREM model's predicted frequency and  $Q$  for  ${}_0S_0$  are 0.81431mHz and 5319, respectively (Dziewonski and Anderson 1981); after the frequency of  ${}_0S_0$  was first determined from the real observations (0.81456mHz in Dratler et al. (1971)), all the related previous studies obtained larger values than the PREM model's predicted value (the estimates given after 2005 are listed in Fig. 6b), except the estimate given by Duan and Huang (2019) based on the NTFT process. In Fig. 6a, we show the normalized power spectra of the 14 SG records for  ${}_0S_0$ . We can see that our estimate (dashed green line) is very close to the highest values of those spectral peaks, while the PREM model's predicted

value (dashed blue line) has a clear difference from them, and the estimate given by Duan and Huang (2019) even has a larger deviation. In addition, Fig. 6c shows that the  $Q$  value given by Duan and Huang (2019) is also the only one that is less than the PREM model's predicted value. In summary, although both this study and Duan and Huang (2019) use the same process to estimate the complex frequency of  ${}_0S_0$  in the time domain, our results are consistent with most of previous studies (Figs. 6b and 6c), while Duan and Huang's (2019) results have clear deviations. This finding further confirms that our NTFT+curve fitting process is better than the NTFT process used in Duan and Huang (2019). We also show related results for  ${}_1S_0$  for further confirmation, and more details can be found in the SI (see Supplementary Figs. S6b and S7).

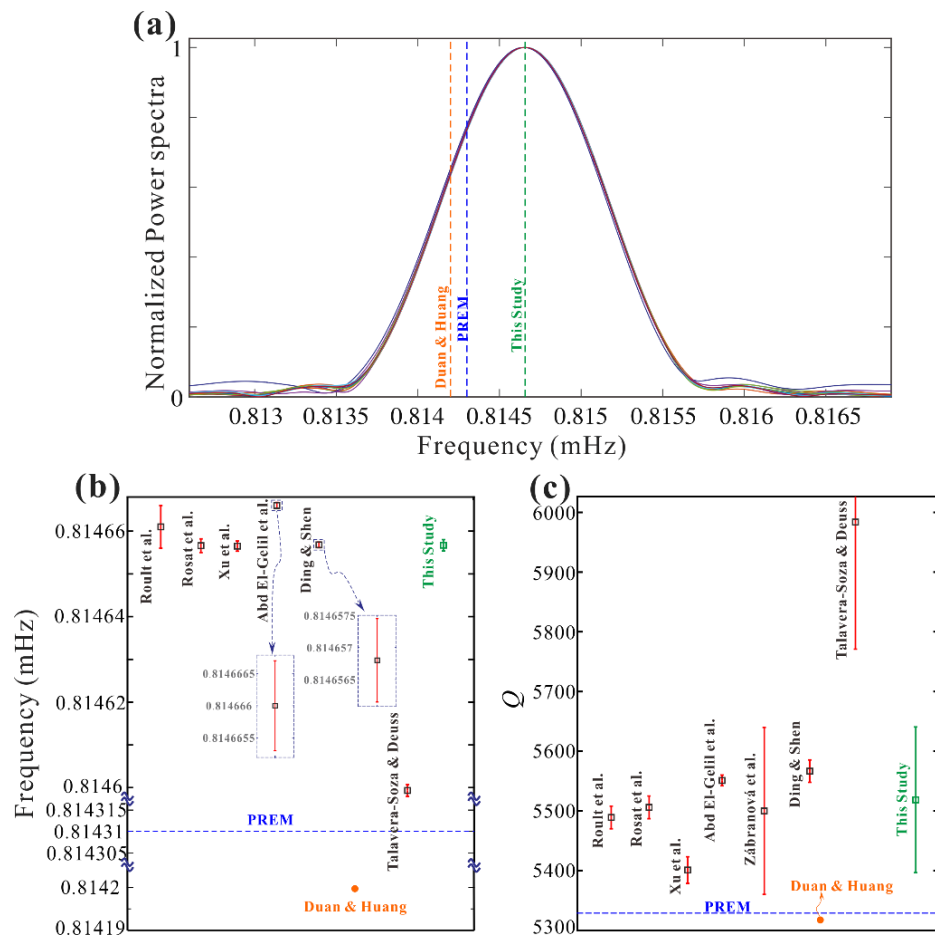


**Figure 6.** (a) The normalization Fourier power spectra of the 14 selected SG records for the  ${}_0S_0$  mode.

(b) Frequency estimates for  ${}_0S_0$  from different studies (Roult et al., 2006; Rosat et al., 2007; Xu et al., 2008; Abd El-Gelil et al., 2010; Zábranová et al., 2012; Ding and Shen, 2014; Duan and Huang, 2019; Talavera-Soza and Deuss, 2021). (c) similar as (b) but for the  $Q$  value.

#### 4 Restoring the interdecadal signals from Earth's rotation variations

After the above verifications, we apply the NTFT+curve fitting process to restore the SYO and EYO from the  $\Delta$ LOD and PM, respectively. Fig. 7a shows the Fourier spectra of the residual PM time series ( $m_1+im_2$ ; 1949/06-2019/06); the red area denotes the background noise level in the  $-0.4$ cpy to  $0.4$ cpy frequency band (calculated after removing the four highest peaks in the  $-0.1$  cpy to  $0.1$ cpy frequency band); the blue areas denote the target  $\pm[0.1, 0.18]$  cpy frequency bands (i.e.,  $\pm[5.5, 10]$  yr period band). We find that only two spectral peaks on the positive axis (in the target frequency bands) are higher than the background noise level, and they correspond to the SYO and EYO. This finding means that both the SYO and EYO in the PM are prograde motions. This finding is slightly different from that of Ding et al. (2019). In Ding et al. (2019), although the  $\sim 8.5$ yr signal was found only on the positive axes of their AR-z spectrum, the  $\sim 5.9$ yr signal was found on both the positive and negative axes. This difference is mainly caused by two reasons: 1) the PM time series used in Ding et al. (2019) did not remove the AAM and OAM effects, so the  $\sim 5$ yr signal caused by the AAM/OAM may have affected the identification of the  $\sim 5.9$ yr signal; 2) Ding et al. (2019) showed the AR-z spectrum of the 1960-2017 PM time series, as they explained that the AR-z spectrum only shows whether a signal exists but does not represent its real amplitude; hence, a very weak harmonic signal may also be found in the AR-z spectrum. In Fig. 7b, we show the NTFT time-frequency spectrum for the SYO obtained from the used residual PM time series. We can see that the main signal of the SYO is presented in the

positive period band, while the negative period band only shows a very weak SYO signal. Hence, the difference between the results of Ding et al. (2019) and this study can be explained. Namely, the SYO is mainly a prograde signal, but given that the Earth is a complex system with triaxial rotation, there is also a slightly retrograde SYO signal. Fig. 7c shows similar results for the EYO, i.e., the EYO is also mainly a prograde signal.

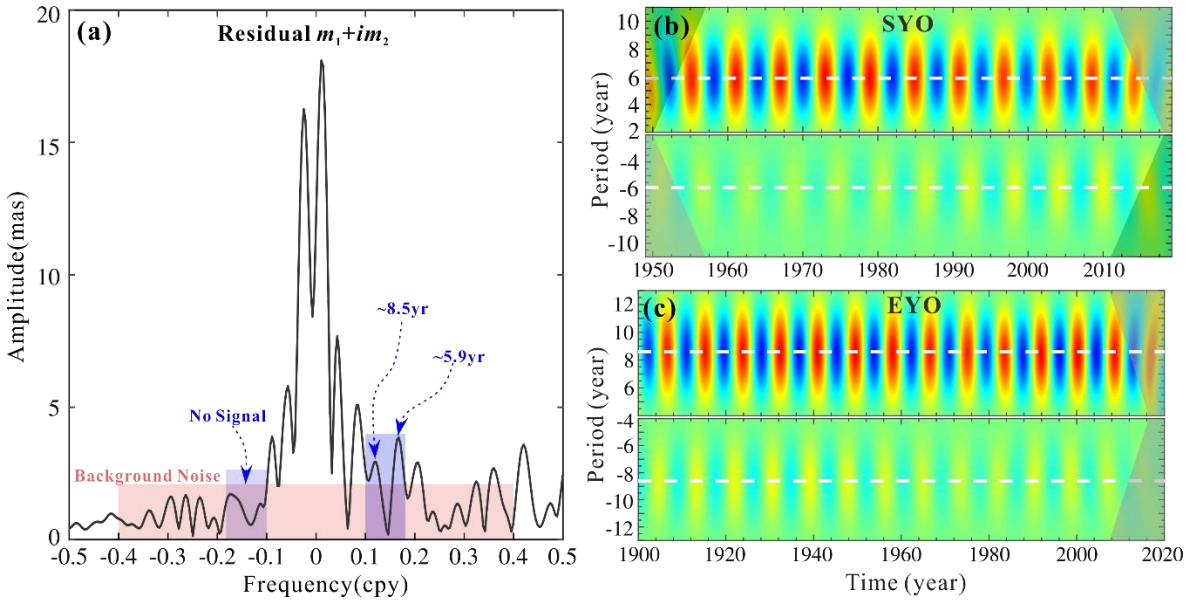


**Figure 7.** (a) The Fourier frequency spectrum of the residual PM ( $m_1+im_2$ ) time series (1949/06-2019/06), in which the AAM and OAM effects have been removed. (b) The prograde and retrograde period-amplitude spectra of the extracted SYO from the residual 1949-2019 PM time series; (c) similar to (b), but for the EYO, which was obtained from the 1861/01-2019/12 yearly EOPC01 PM time series (only showing the results after 1900).

Fig. 8 further shows the restored time-varying SYO and EYO from the  $\Delta\text{LOD}$  and the  $m_1/m_2$  components of the PM. Fig. 8a shows the restored SYOs, and the SYO result obtained from the  $\Delta\text{LOD}$  given by Ding et al. (2021) is also shown (purple curve). Note that the restored SYO from the  $m_1$  component of the PM was moved forward by  $\sim 1.5\text{yr}$  ( $\pi/2$  phase), and the  $m_2$  component of the PM was

multiplied by minus 1. We can see that all four curves are very close (except for the end parts), except that the 1962-1974 parts of the results obtained by Ding et al. (2021) were affected by the edge effect of the filter. Fig. 8b shows the restored EYOs; the EYO obtained from the  $\Delta\text{LOD}$  given by Ding et al. (2021) is also plotted, and the restored EYO from the  $m_2$  component of the PM was moved forward by  $\sim 2.1\text{yr}$  ( $\pi/2$  phase). Better than the results for the SYO in Fig. 8a, the four curves in Fig. 8b are very consistent with each other. Fig. 8 reconfirms that both the SYO and EYO in the  $\Delta\text{LOD}$  have time-varying amplitudes in the time domain, which are the same as those in Ding et al. (2021), but different from the findings given by Duan and Huang (2020) (stable decayed SYO and increased EYO were obtained). The most important thing is that, for the first time, we find that the SYO/EYO contained in PM and  $\Delta\text{LOD}$  have good consistency. This finding undoubtedly helps us understand the physical mechanisms of the SYO and EYO in the Earth system.

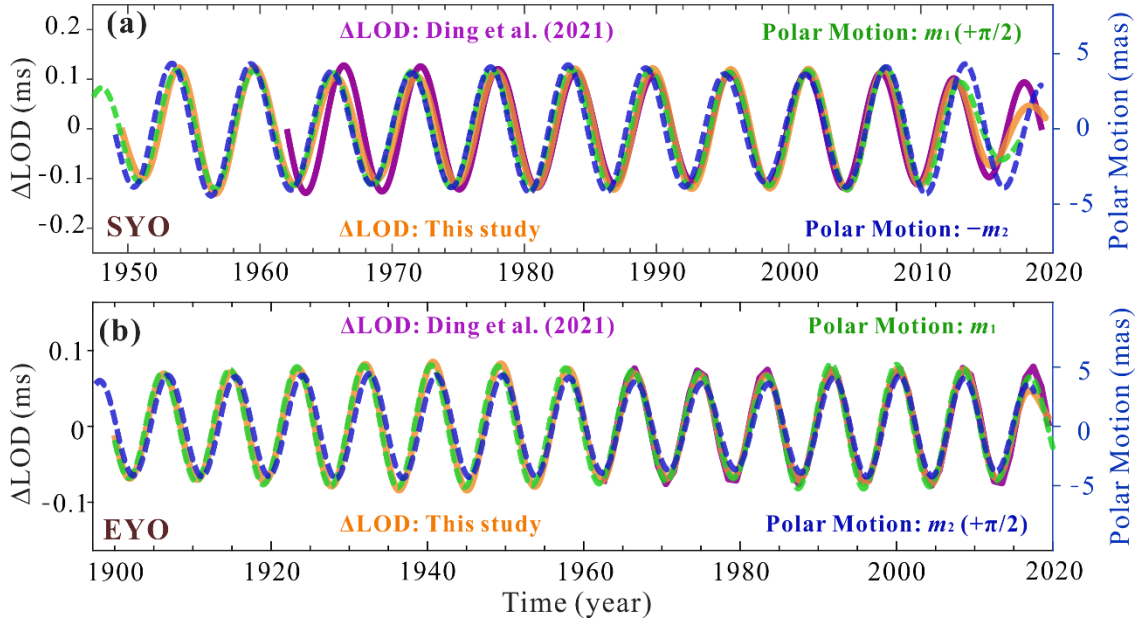


**Figure 8.** (a) The restored SYOs from the 1949-2019 residual  $\Delta\text{LOD}$  (yellow curve), Ding et al. (2021) (purple curve), and the  $m_1$  and  $m_2$  components of the 1949-2019 PM time series; the result for  $m_1$  was moved forward by  $\pi/2$  phase, and the result for  $m_2$  was multiplied by minus 1. (b) similar to (a), but

for EYOs from the original 1860/06-2019/06 yearly  $\Delta$ LOD record and the original 1861/01-2019/12 yearly EOPC01 PM time series; the result for  $m_2$  was also moved forward by  $\pi/2$  phase.

## 5. Discussions and Conclusions

To use the NTFT to restore the SYOs and EYOs from the  $\Delta$ LOD and PM time series, we use a curve fitting process to remove the other unconcerned signals to improve the frequency resolution of the NTFT. The validity and superiority of the NTFT+curve fitting scheme were confirmed by simulated tests and real observations. Then, we use the NTFT+curve fitting scheme to process the  $\Delta$ LOD and PM time series, and we reconfirm that both the SYOs and EYOs have time varying amplitudes (same as the findings in Holme and de Viron (2013), Ding (2019) and Ding et al. (2021)) but not stable damping amplitudes (given by Duan et al. (2015) and Duan and Huang (2020)) in the time domain. Furthermore, for the first time, we find that the SYOs/EYOs contained in the  $\Delta$ LOD and PM have good consistency. The SYO in the  $m_1$  component of the PM has a phase deviation of  $\sim\pi/2$  from that in the  $m_2$  component, and the same situation hold for EYO. Considering that the directions of  $m_1$  and  $m_2$  have a  $\pi/2$  angle difference in the equatorial plane, such findings are understood.

The remaining problem is to determine why the SYOs/EYOs in LOD and PM have good consistency. Such consistency can hardly be construed as unrelated phenomena or mere fortuitous coincidence, which strongly suggests a common excitation source. Given that the three main external excitation sources of the  $\Delta$ LOD and PM have no significant SYO or EYO signal, we tend to believe that the sources of SYOs/EYOs should be in Earth's interior. It has been suggested that the  $\Delta$ LOD and PM variations are coupled when considering the interaction between the core flow and a realistic nonaxial, nondipolar magnetic field; such an interaction produces both axial and equatorial torques on

the inner core and mantle (Dumberry and Bloxham, 2002; Mound and Buffett, 2005; Nakada, 2006). Chen et al. (2019) suggested that the possible source of the SYO should be in the Earth's interior and probably from the core. Ding and Chao (2018a) suggested a mantle-inner core gravitational (MICG) coupling mechanism for the SYO in  $\Delta$ LOD (also suggested by Mound and Buffett (2003)), but it cannot be used to explain the SYO in the PM. Dumberry (2008) studied the influence of the inner core in the PM by examining the gravitational coupling between the inner core and density heterogeneities in the mantle. Although his model cannot simultaneously explain the observed decadal changes in  $\Delta$ LOD and PM, it may still have the potential to explain the interdecadal changes in them (the amplitudes of the SYO and EYO in the PM are only  $\sim$ 3-5mas). Based on numerical geodynamo simulations, Kuang et al. (2019) also showed that electromagnetic core-mantle coupling is sufficiently strong to excite decadal PM to magnitudes of  $\sim$ 10mas.

We do not try to provide a detailed possible mechanism for the observed SYOs/EYOs in the Earth's rotation variations, and we believe that this will remain a problem in years to come. Instead, based on this first consistency between interdecadal changes in the  $\Delta$ LOD and PM, we suggest that the Earth's inner core may play an important role in their physical interpretations.

## Acknowledgements

The used  $\Delta$ LOD and PM data can be downloaded from IERS ([www.iers.org/IERS/EN/DataProducts/EarthOrientationData/eop.html](http://www.iers.org/IERS/EN/DataProducts/EarthOrientationData/eop.html)); The AAM, OAM and HAM datasets were downloaded from: [www.iers.org/IERS/EN/DataProducts/GeophysicalFluidsData/geoFluids.html](http://www.iers.org/IERS/EN/DataProducts/GeophysicalFluidsData/geoFluids.html). The superconducting gravimeter (SG) records can be downloaded from: [www.eas.slu.edu/GGP/tohoku2011.html](http://www.eas.slu.edu/GGP/tohoku2011.html). This work

is supported by NSFC (grant # 41721003, 41974022, 41774024) and by Educational Commission of Hubei Province of China (grant #2020CFA109).

## References

Abd El-Gelil, M., Pagiatakis, S., & El-Rabbany, A. (2010). Normal mode detection and splitting after Sumatra–Andaman earthquake. *Journal of Geodynamics*, 50(2), 49-56. <https://doi.org/10.1016/j.jog.2010.02.003>

Barnes, R. T. H., Hide, R., White, A. A., & Wilson, C. A. (1983). Atmospheric angular momentum fluctuations, length-of-day changes and polar motion. *Proceedings of the Royal Society of London. A. Mathematical and Physical Sciences*, 387(1792), 31-73. <https://doi.org/10.1098/rspa.1983.0050>

Bizouard, C. . (2018). Continental drift of the rotation pole: observation and theory. *IOP Conference Series Materials Science and Engineering*, 468(1), 012005.

Bizouard, C., Lambert, S., Gattano, C., & Becker, C. (2019). The IERS EOP 14C04 solution for Earth orientation parameters consistent with ITRF 2014. *Journal of Geodesy*, 93, 621– 633. <https://doi.org/10.1007/s00190-018-1186-3>

Cai, S., Liu, L., & Wang, G. (2018). Short-term tidal level prediction using normal time-frequency transform. *Ocean Engineering*, 156, 489-499. <https://doi.org/10.1016/j.oceaneng.2018.03.021>

Chen, J., Wilson, C. R., Kuang, W., & Chao, B. F. (2019). Interannual oscillations in Earth rotation. *Journal of Geophysical Research: Solid Earth*, 124, 13404– 13414. <https://doi.org/10.1029/2019JB018541>

Cohen, L. (1989). Time-frequency distributions-a review. *Proceedings of the IEEE*, 77(7), 941-981. <https://doi.org/10.1109/5.30749>

Cohen, L. (1995). *Time-frequency analysis* (Vol. 778). Englewood Cliffs, NJ: Prentice Hall PTR.

Cui, X., Sun, H., Xu, J., Zhou, J., & Chen, X. (2020). Relationship between free core nutation and geomagnetic jerks. *Journal of Geodesy*, 94(4), 1-13. <https://doi.org/10.1007/s00190-020-01367-7>

Ding, H. (2019). Attenuation and excitation of the ~6-year oscillation in the length-of-day variation. *Earth and Planetary Science Letters*, 507, 131– 139. <https://doi.org/10.1016/j.epsl.2018.12.003>

Ding, H., An, Y., & Shen, W. (2021). New evidence for the fluctuation characteristics of intradecadal periodic signals in length-of-day variation. *Journal of Geophysical Research: Solid Earth*, 126, e2020JB020990. <https://doi.org/10.1029/2020JB020990>

Ding, H., Pan, Y. J., Xu, X. Y., Shen, W., & Li, M. (2019). Application of the AR-z spectrum to polar motion: A possible first detection of the inner core wobble and its implications for the density of Earth's core. *Geophysical Research Letters*, 46, 13765– 13774. <https://doi.org/10.1029/2019GL085268>

Ding, H., & Chao, B. F. (2018a). A 6-year westward rotary motion in the Earth: Detection and possible MICG coupling mechanism. *Earth and Planetary Science Letters*, 495, 50-55. <https://doi.org/10.1016/j.epsl.2018.05.009>

Ding, H., & Chao, B. F. (2018b). Application of stabilized AR-z spectrum in harmonic analysis for geophysics. *Journal of Geophysical Research: Solid Earth*, 123, 8249– 8259. <https://doi.org/10.1029/2018JB015890>

Ding, H., & Shen, W. B. (2014). Determination of the complex frequencies for the normal modes below 1mHz after the 2010 Maule and 2011 Tohoku earthquakes. *Annals of Geophysics*, 56(5),

0563. <https://doi.org/10.4401/ag-6400>

Dratler, J., Farrell, W. E., Block, B., & Gilbert, F. (1971). High-Q overtone modes of the Earth. *Geophysical Journal International*, 23(4), 399-410. <https://doi.org/10.1111/j.1365-246X.1971.tb01832.x>

Duan, P., & Huang, C. (2019). Application of normal Morlet wavelet transform method to the damped harmonic analysis: on the isolation of the seismic normal modes ( ${}_0S_0$  and  ${}_0S_5$ ) in time domain. *Physics of the Earth and Planetary Interiors*, 288, 26-36. <https://doi.org/10.1016/j.pepi.2019.01.005>

Duan, P., & Huang, C. (2020). Intradecadal variations in length of day and their correspondence with geomagnetic jerks. *Nature communications*, 11(1), 1-8. <https://doi.org/10.1038/s41467-020-16109-8>

Duan, P., Liu, G., Liu, L., Hu, X., Hao, X., Huang, Y., ... & Wang, B. (2015). Recovery of the 6-year signal in length of day and its long-term decreasing trend. *Earth, Planets and Space*, 67(1), 1-11. <https://doi.org/10.1186/s40623-015-0328-6>

Dumberry, M., & Bloxham, J. (2002). Inner core tilt and polar motion. *Geophysical Journal International*, 151(2), 377-392. <https://doi.org/10.1046/j.1365-246X.2002.01756.x>

Dumberry, M. (2008). Gravitational torque on the inner core and decadal polar motion. *Geophysical Journal International*, 172(3), 903-920. <https://doi.org/10.1111/j.1365-246X.2007.03653.x>

Dziewonski, A. M., & Anderson, D. L. (1981). Preliminary reference Earth model. *Physics of the earth and planetary interiors*, 25(4), 297-356. [https://doi.org/10.1016/0031-9201\(81\)90046-7](https://doi.org/10.1016/0031-9201(81)90046-7)

Eubanks, T. M. (1993). Variations in the orientation of the Earth. *Contributions of space geodesy to geodynamics: Earth dynamics*, 24, 1-54. <https://doi.org/10.1029/GD024p0001>

Gross, R. S. (1993). The effect of ocean tides on the Earth's rotation as predicted by the results of an ocean tide model. *Geophysical research letters*, 20(4), 293-296.

<https://doi.org/10.1029/93GL00297>

Gross, R. S. (2015). In: Earth rotation variations-long period. *Treatise on geophysics* ( 2<sup>nd</sup> ed.), 3. 215– 261. <https://doi.org/10.1016/B978-044452748-6.00057-2>

Holme, R., & de Viron, O. (2013). Characterization and implications of intradecadal variations in length of day. *Nature*, 499(7457), 202– 204. <https://doi.org/10.1038/nature12282>

Kuang, W., Chao, B. F., & Chen, J. (2019). Reassessment of electromagnetic core-mantle coupling and its implications to the Earth's decadal polar motion. *Geodesy and Geodynamics*, 10(5), 356-362. <https://doi.org/10.1016/j.geog.2019.06.003>

Liu, L., & Hsu, H. (2009). Time–frequency transform: inversion and normalization. *Hubei Science and Technology Press, Hubei*.

Liu, L., & Hsu, H. (2011, July). Inversion and normalization of time-frequency transform. In *2011 international conference on multimedia technology* (pp. 2164-2168). IEEE.

Liu, L., Hsu, H., & Grafarend, E. W. (2007). Normal Morlet wavelet transform and its application to the Earth's polar motion. *Journal of Geophysical Research: Solid Earth*, 112(B8). <https://doi.org/10.1029/2006JB004895>

Modiri, S., Belda, S., Hoseini, M., Heinkelmann, R., Ferrández, J. M., & Schuh, H. (2020). A new hybrid method to improve the ultra-short-term prediction of LOD. *Journal of geodesy*, 94(2), 1-14. <https://doi.org/10.1007/s00190-020-01354-y>

Mound, J. E., & Buffett, B. A. (2003). Interannual oscillations in length of day: Implications for the structure of the mantle and core. *Journal of Geophysical Research: Solid Earth*, 108(B7).

<https://doi.org/10.1029/2002JB002054>

Mound, J. E., & Buffett, B. A. (2005). Mechanisms of core-mantle angular momentum exchange and the observed spectral properties of torsional oscillations. *Journal of Geophysical Research: Solid Earth*, 110(B8). <https://doi.org/10.1029/2004JB003555>

Munk, W. H., & MacDonald, G. J. (1960). The rotation of the earth; a geophysical discussion. *Cambridge [Eng.] University Press*.

Nakada, M. (2006). Axial and equatorial rotations of the Earth's cores associated with the Quaternary ice age. *Physics of the Earth and Planetary Interiors*, 154(2), 113-147.

<https://doi.org/10.1016/j.pepi.2005.08.004>

Rosat, S., Watada, S., & Sato, T. (2007). Geographical variations of the  $0S_0$  normal mode amplitude: predictions and observations after the Sumatra-Andaman earthquake. *Earth, planets and space*, 59(4), 307-311. <https://doi.org/10.1186/BF03353109>

Roult, G., Rosat, S., Clévédé, E., Millot-Langet, R., & Hinderer, J. (2006). New determinations of Q quality factors and eigenfrequencies for the whole set of singlets of the Earth's normal modes  $0S_0$ ,  $0S_2$ ,  $0S_3$  and  $2S_1$  using superconducting gravimeter data from the GGP network. *Journal of Geodynamics*, 41(1-3), 345-357. <https://doi.org/10.1016/j.jog.2005.08.020>

Stephenson, F. R., & Morrison, L. V. (1985). Non-tidal changes in the length of the day: 700 BC to AD 1982. *Geophysical Surveys*, 7, 201– 210. <https://doi.org/10.1007/BF01450890>

Su, X., Liu, L., Houtse, H., & Wang, G. (2014). Long-term polar motion prediction using normal time-frequency transform. *Journal of Geodesy*, 88(2), 145-155. <https://doi.org/10.1007/s00190-013-0675-7>

Talavera-Soza, S., & Deuss, A. (2021). New measurements of long-period radial modes using large

earthquakes. *Geophysical Journal International*, 224(2), 1211-1224.

<https://doi.org/10.1093/gji/ggaa499>

Vautard, R., Yiou, P., & Ghil, M. (1992). Singular-spectrum analysis: A toolkit for short, noisy chaotic signals. *Physica D: Nonlinear Phenomena*, 58(1-4), 95-126. [https://doi.org/10.1016/0167-2789\(92\)90103-T](https://doi.org/10.1016/0167-2789(92)90103-T)

Wahr, J. M. (1985), Deformation induced by polar motion, *J. Geophys. Res.*, 90( B11), 9363–9368, <https://doi.org/10.1029/JB090iB11p09363>

Walwer, D., Calais, E., & Ghil, M. (2016). Data-adaptive detection of transient deformation in geodetic networks. *Journal of Geophysical Research: Solid Earth*, 121(3), 2129-2152. <https://doi.org/10.1002/2015JB012424>

Xu, Y., Crossley, D., & Herrmann, R. B. (2008). Amplitude and Q of 0S0 from the Sumatra earthquake as recorded on superconducting gravimeters and seismometers. *Seismological Research Letters*, 79(6), 797-805. <https://doi.org/10.1785/gssrl.79.6.797>

Zábranová, E., Matyska, C., Hanyk, L., & Pálinkáš, V. (2012). Constraints on the centroid moment tensors of the 2010 Maule and 2011 Tohoku earthquakes from radial modes. *Geophysical research letters*, 39(18). <https://doi.org/10.1029/2012GL052850>

Zotov, L. (2019). Length of Day Analysis, 6-year Signal and Edge Effects, talk at AOGS-2019, SE10-A013, Singapore.

# The consistency of interdecadal changes in the Earth's rotation variations

Yachong An, Hao Ding\*, Zhifeng Chen

*Department of Geophysics, School of Geodesy and Geomatics, Key Laboratory of Geospace Environment and Geodesy of the Ministry of Education, Wuhan University, 430079, Wuhan, China*

\*Corresponding address: [dhaosgg@sgg.whu.edu.cn](mailto:dhaosgg@sgg.whu.edu.cn)

## Contents of this file

### Materials and Methods:

1. The simulated tests
2. Why does the BEPME strategy obtain strange waveforms?
3.  $Q$  value and frequency of the  ${}_0S_0$  and  ${}_1S_0$

**Figure S1.** Synthesized noisy time series and simulated tests for the NTFT.

**Figure S2.** The synthetic test for the validation of the NTFT+curve fitting process.

**Figure S3.** Explanations for why BEPME will obtain strange signal in time domain.

**Figure S4.** Explanations for why BEPME will obtain strange signal in time-frequency domain.

**Figure S5.** The extracted  ${}_0S_0/{}_1S_0$  modes from some stations.

**Figure S6.** The calculated  $Q$  value and frequency of  ${}_0S_0/{}_1S_0$  mode for each station.

**Figure S7.** The normalization Fourier power spectra of the selected stations, and the frequency and  $Q$  estimates from different studies for  ${}_1S_0$ .

### 1. The simulated tests

In Fig. S1a, we use three harmonics ( $s_1(t)=\cos(2\pi/9t-0.156)$ ,  $s_2(t)=1.2\cos(2\pi/11t+1.8)$  and  $s_3(t)=\cos(2\pi/15t-0.68)$ ) with different random noises to synthesize four time series,  $\mathbf{x}_1$  ( $=s_1(t)+\text{noise}$ ),  $\mathbf{x}_2$  ( $=s_2(t)+\text{noise}$ ),  $\mathbf{x}_3$  ( $=s_3(t)+\text{noise}$ ) and  $\mathbf{x}$  ( $=s_1(t)+s_2(t)+s_3(t)+\text{noise}$ ). Here we use a 0.05s sampling interval, and the lengths of those time series are the same 70s. Fig. S1b shows that the restored time series (red curves) from  $\mathbf{x}_1$ ,  $\mathbf{x}_2$  and  $\mathbf{x}_3$  are almost the same as those input oscillations (gray curves), but the restored  $s_i$  ( $i=1, 2$  and  $3$ ) from  $\mathbf{x}(t)$  are clearly different (green curves) with their corresponding input signals. This demonstrates that the NTFT can extract harmonics from a simply noisy time series but has no enough frequency resolution to restore target signal from more complicated time series when the available length is limited.

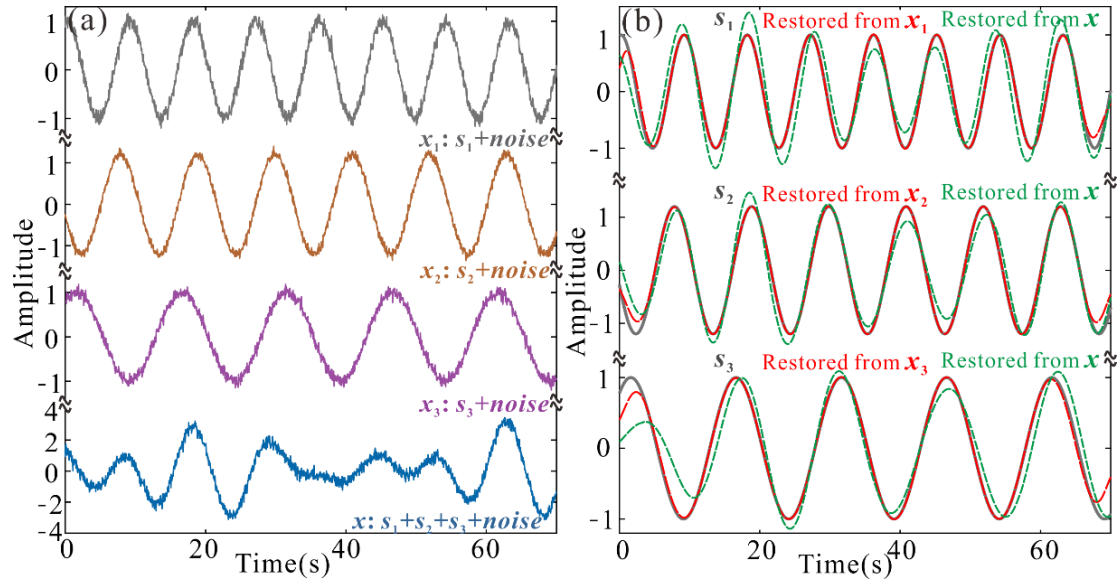


**Fig. S1.** (a) Synthesized noisy time series  $x_1$ ,  $x_2$ ,  $x_3$  and  $x$ . (b) Simulated (gray curves) and restored  $s_1$ ,  $s_2$ , and  $s_3$  from  $x_1$ ,  $x_2$ ,  $x_3$  (red curves) and  $x$  (green curves) using the NTFT, respectively.

Fig. S2 further shows the restored results from  $x(t)$  based on the NTFT+ BEPME strategy and our new scheme, respectively (the results from NTFT are also re-plotted for comparisons). The results from the NTFT+ BEPME strategy (red curves) have clearly deviations with the input signal (we will explain reasons latter), the restored  $s_3$  even has stable increasing amplitude (see Fig. S2c). Fig. S2 denotes that restored results of the NTFT+ curve fitting (yellow curves) are good consistent with the input signals. These simulated tests preliminarily confirmed the relative advantages of our new strategy.

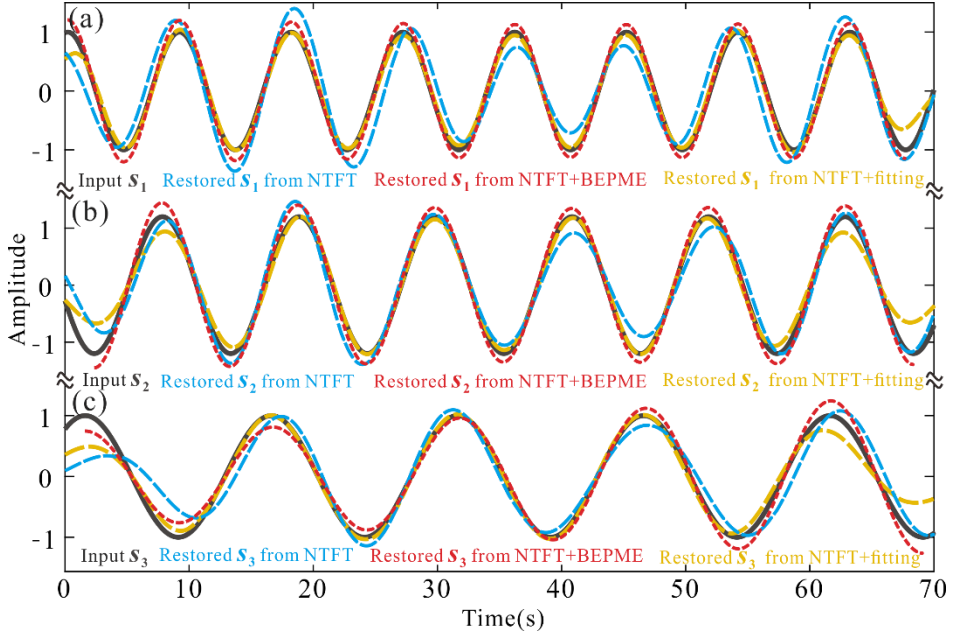


**Fig. S2.** The restored  $s_i$  ( $i=1, 2, 3$ ) based on NTFT, NTFT+BEPME and NTFT+curve fitting strategies; the input signals are also plotted. (a) for  $s_1$ ; (b) for  $s_2$ ; and (c) for  $s_3$ .

## 2. Why does BEPME strategy obtain strange waveforms?

Given that the NTFT+BEPME strategy has been used in several previous studies (Duan et al. 2015, 2017 and 2018; Duan and Huang, 2020), and Ding et al. (2021) have found that the NTFT+BEPME strategy restored stable damping amplitudes for the input cosine signals. Here we will further give a simply explanation about why the BEPME strategy will obtain strange waveforms. Still taking the time series  $\mathbf{x}=s_1+s_2+s_3$  (same as test in Fig. S2 but without noise) as example, if we want to restore  $s_1$  from complicated time series with close frequency signals; for simplistic, supposing that the estimated extreme points for  $s_1$  are ideally very close to the real extreme points of  $s_1$  ( $t_1$  and  $t_2$  as shown in Fig. S3a), after using the BEPME process, the result is shown as Fig. S3b. If there is only single signal  $s_1$  in  $\mathbf{x}$ , Fig. S3b shows that the extended time series is quite well; however, there are still some other signals (here are  $s_2$  and  $s_3$ ). As an independent recovery process for  $s_1$ , when we use the estimated extreme points to extend the time series  $\mathbf{x}$ , the contained  $s_2$  and  $s_3$  will be also extended. Given that the real extreme points of  $s_2$  and  $s_3$  (see as  $t_3$ , and  $t_4$  in Fig. S3a) will not same as those of  $s_1$ , the extended results for them will have singular values (see pink shaded area in Fig. S3a). Accordingly, the extended time series for  $\mathbf{x}$  will also have singular values (see pink shaded area in Fig. S3a). Fig. S3b shows the restored  $s_1$  from the extended  $\mathbf{x}$ , we can see that a stable damping result was obtained, even the input

$s_1$  is stable cosine signal. Fig.S3b also shows that a weak  $s_1$  signal were restored from the extended  $s_2+s_3$  time series, even there is no  $s_1$  signal in input signals, and this restored time series is very close to the difference between the restored  $s_1$  from the extended  $x$  and its corresponding input  $s_1$  signal. In Fig. S4, we show two period-amplitude spectra, the first one is for the extended  $s_2+s_3$  time series (Fig. S4a), and the second one is a residual spectrum. As we have known the functions for  $x$ , so we can exactly calculate its corresponding values in the two extended bands, then the period-amplitude spectra  $P_1$  can be obtained by using the NTFT, while  $P_2$  denotes the period-phase spectrum of the extended  $x$  by using BEPME. Fig. S4b just shows the residual results of  $P_2-P_1$ . Comparing the two period-amplitude spectra of Fig. S4 in the  $t_1-t_2$  time span, we can find that they are very close to each other. This finding further explain that the singular values of the un-target signal caused by the BEPME process will distort the final result.

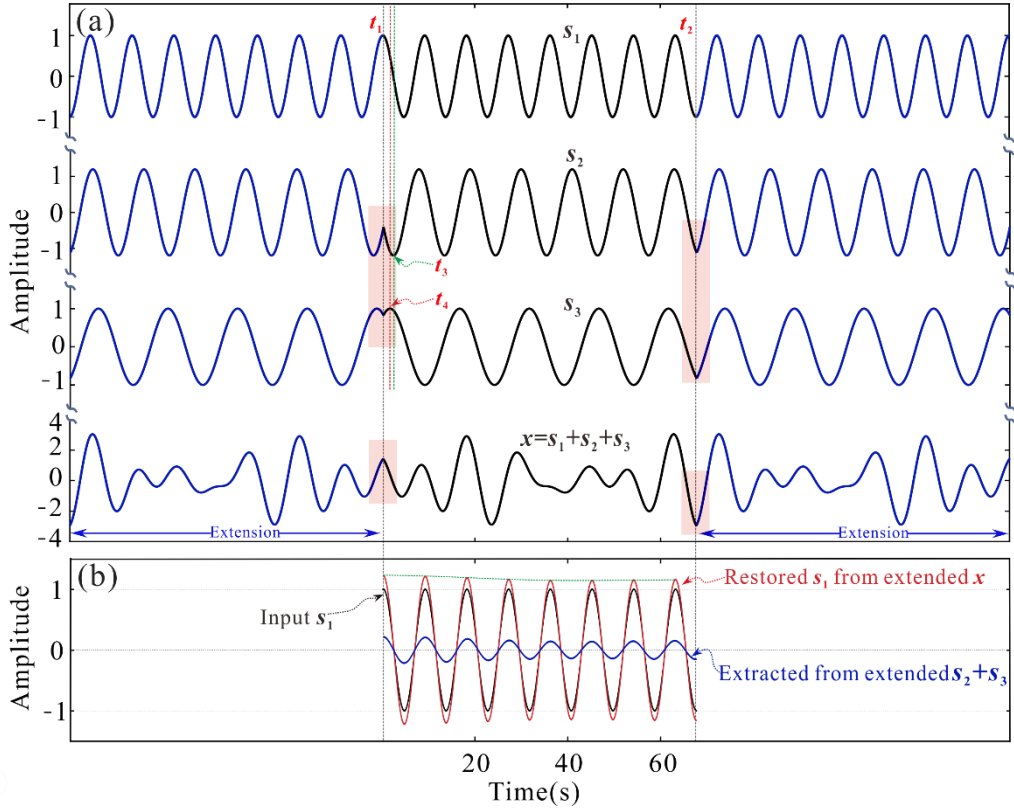


**Fig. S3.** (a) The mirror extension of  $s_1$ ,  $s_2$ ,  $s_3$  and  $s_1+s_2+s_3$  according to extreme points of  $s_1$  at both ends; extreme points and singular values (pink shaded area). (b) Input  $s_1$  (black curve) and extracted  $s_1$  from extended  $x$  (red curve) and extended  $s_2+s_3$  (blue curve).

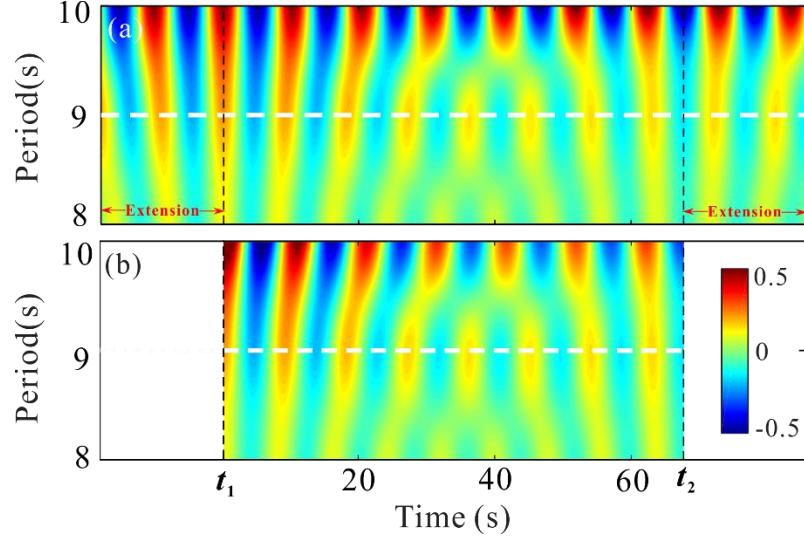


**Fig. S4.** (a) The period-amplitude spectra of the time series extended  $s_2+s_3$ . (b) The residuals between the period-amplitude spectra of the extended  $x$  (by BEPME) and of the real  $x$  (for the same extended time span). Black dashed lines denote the extension axis of symmetry, and white dashed lines denote the periods of target of harmonics.

### 3. $Q$ value and frequency of the ${}_0S_0$ and ${}_1S_0$

In this study, we use SG records from different stations, listing as Schiltach (b1, b2), Canberra (cb), Conrad (co), Djougou (dj), Bad Homburg (h1, h2, h3), Moxa (m1, m2), Membach (mb), Medicina (mc), Pecny (pe), Strasbourg (st), and Wettzell (w3, w4). Fig. S5 shows the clear damping decaying trend in the extracted  ${}_0S_0$  and  ${}_1S_0$  modes by our NTFT+curve fitting process (only show some stations). The calculated  $Q$  values and frequencies for each station and their corresponding weighted mean are shown in Fig. S6; the estimated errors are calculated by the bootstrap method (Efron & Tibshirani 1986). We obtain the final frequency of  $0.8146567 \pm 1.3e-6$  mHz and the  $Q$  value of  $5518 \pm 122$  for the  ${}_0S_0$  mode, the final frequency of  $1.631563 \pm 1.22e-5$  mHz and the  $Q$  value of  $1978 \pm 91$  for the  ${}_1S_0$  mode.

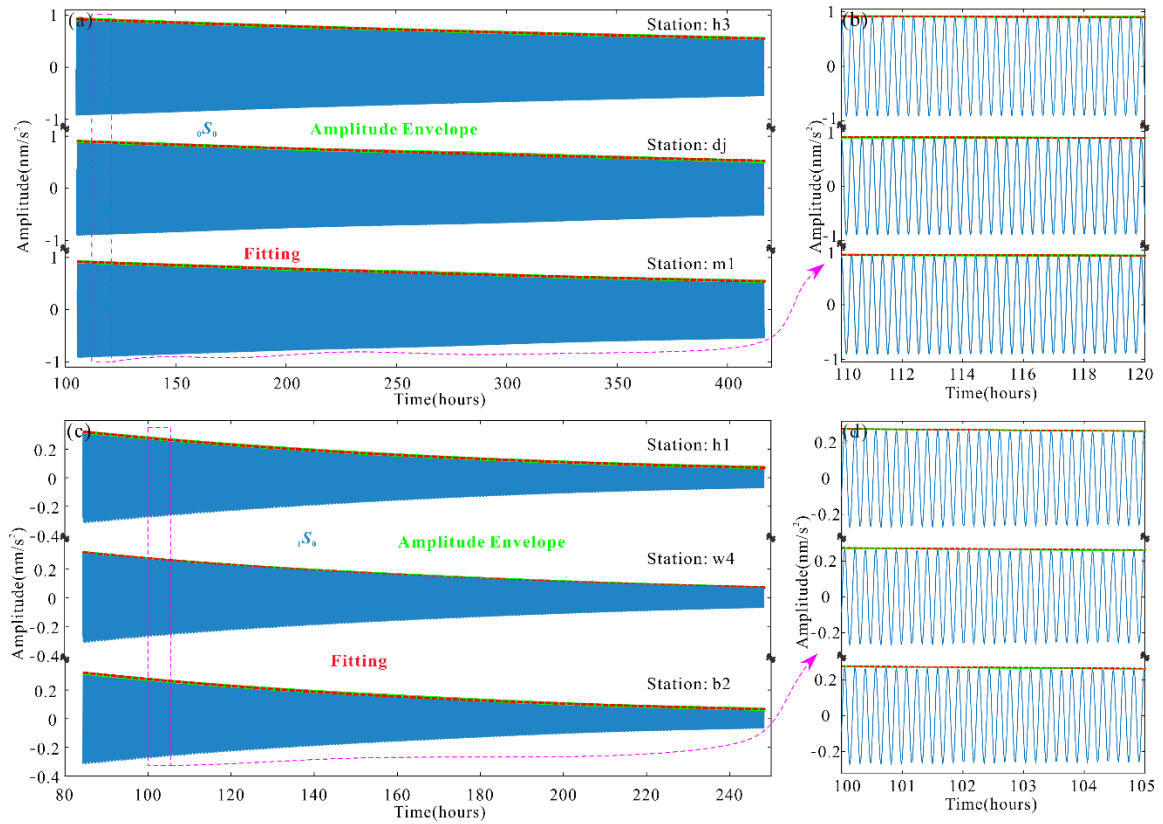


**Fig. S5** (a) The extracted  ${}_0S_0$  modes are from h3, dj and m1 station. (c) Similar to (a) but for the  ${}_1S_0$  modes from h1, w4 and b2 station. (b) and (d) are the local magnifications of (a) and (c), respectively. The blue curves denote extracted modes, the light green curves denote their amplitude envelopes and the red curves denote fitted envelopes.

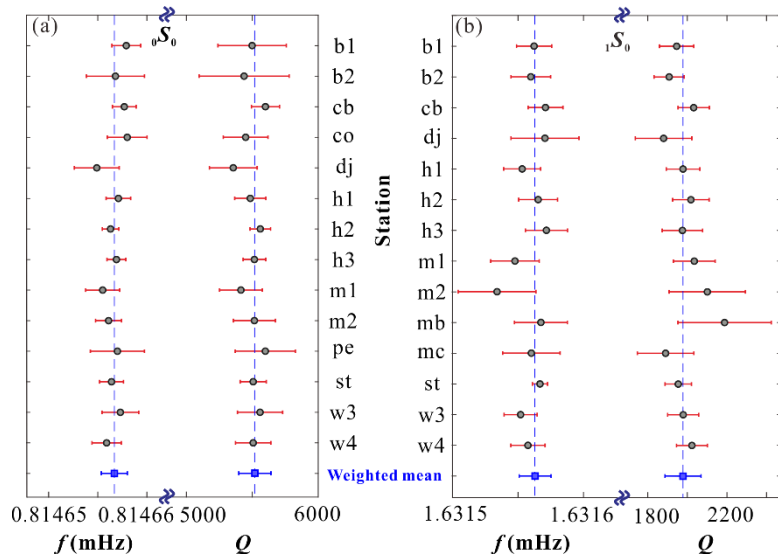


**Fig. S6.** (a) The calculated  $Q$  values and frequencies of  ${}_0S_0$  mode in each station (black circle) and their weighted means (blue rectangle). (b) Similar to (a) but for the  ${}_1S_0$  mode.

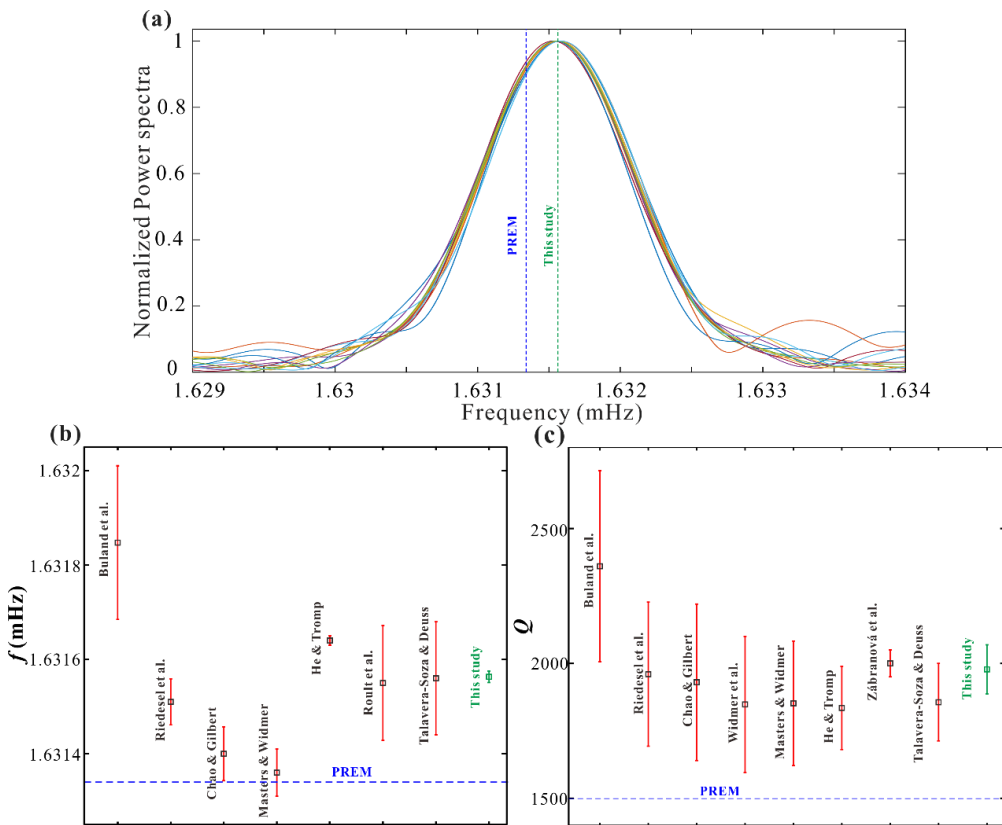


**Fig. S7.** (a) The normalization Fourier power spectra of the 14 selected SG records for the  $1S_0$  mode. (b) the frequency estimates for  $1S_0$  from different studies (Buland et al., 1979; Riedesel et al., 1980; Chao & Gilbert, 1980; Widmer et al., 1991; Masters & Widmer, 1995; He & Tromp, 1996; Roult et al., 2010; Zábranová et al., 2017; Talavera-Soza & Deuss, 2021). (c) similar as (b) but for the  $Q$  value.

Fig. S7 compares the final results of the  $1S_0$  mode with those of previous studies and the theoretical predictions of PREM (Dziewonski & Anderson 1981). Fig. S7a shows the PREM model's predicted value is smaller, and Fig. S7b also confirm this. Fig. S7b and 7c show that there is good consistency in previous results for the  $1S_0$  mode and our result almost falls within the error limits of previous studies. Through the above comparison, the validity and reliability of our new scheme are further verified.

## Reference

Buland, R., Berger, J., & Gilbert, F. (1979). Observations from the IDA network of attenuation and splitting during a recent earthquake. *Nature*, 277(5695), 358-362. <https://doi.org/10.1038/277358a0>

Chao, B. F., & Gilbert, F. (1980). Autoregressive estimation of complex eigenfrequencies in low

frequency seismic spectra. *Geophysical Journal International*, 63(3), 641-657. <https://doi.org/10.1111/j.1365-246X.1980.tb02643.x>

Ding, H., An, Y., & Shen, W. (2021). New evidence for the fluctuation characteristics of intradecadal periodic signals in length-of-day variation. *Journal of Geophysical Research: Solid Earth*, 126, e2020JB020990. <https://doi.org/10.1029/2020JB020990>

Dziewonski, A. M., & Anderson, D. L. (1981). Preliminary reference Earth model. *Physics of the earth and planetary interiors*, 25(4), 297-356. [https://doi.org/10.1016/0031-9201\(81\)90046-7](https://doi.org/10.1016/0031-9201(81)90046-7)

Duan, P., Liu, G., Liu, L., Hu, X., Hao, X., Huang, Y., ... & Wang, B. (2015). Recovery of the 6-year signal in length of day and its long-term decreasing trend. *Earth, Planets and Space*, 67(1), 1-11. <https://doi.org/10.1186/s40623-015-0328-6>

Duan, P., Liu, G., Hu, X., Sun, Y., & Li, H. (2017). Possible damping model of the 6 year oscillation signal in length of day. *Physics of the Earth and Planetary Interiors*, 265, 35-42. <https://doi.org/10.1016/j.pepi.2017.02.002>

Duan, P., Liu, G., Hu, X., Zhao, J., & Huang, C. (2018). Mechanism of the interannual oscillation in length of day and its constraint on the electromagnetic coupling at the core–mantle boundary. *Earth and Planetary Science Letters*, 482, 245-252. <https://doi.org/10.1016/j.epsl.2017.11.007>

Duan, P., & Huang, C. (2020). Intradecadal variations in length of day and their correspondence with geomagnetic jerks. *Nature communications*, 11(1), 1-8. <https://doi.org/10.1038/s41467-020-16109-8>

Efron, B., & Tibshirani, R. (1986). Bootstrap methods for standard errors, confidence intervals, and other measures of statistical accuracy. *Statistical science*, 54-75.

He, X., & Tromp, J. (1996). Normal-mode constraints on the structure of the Earth. *Journal of Geophysical Research: Solid Earth*, 101(B9), 20053-20082. <https://doi.org/10.1029/96JB01783>

Masters, T. G., & Widmer, R. (1995). Free oscillations: frequencies and attenuations. *Global Earth Physics: a handbook of physical constants*, I, 104. <https://doi.org/10.1029/RF001>

Riedesel, M. A., Agnew, D., Berger, J., & Gilbert, F. (1980). Stacking for the frequencies and Q s of 0 S 0 and 1 S 0. *Geophysical Journal International*, 62(2), 457-471. <https://doi.org/10.1111/j.1365-246X.1980.tb04867.x>

Roult, G., Roch, J., & Clévédé, E. (2010). Observation of split modes from the 26th December 2004 Sumatra-Andaman mega-event. *Physics of the Earth and Planetary Interiors*, 179(1-2), 45-59. <https://doi.org/10.1016/j.pepi.2010.01.001>

Talavera-Soza, S., & Deuss, A. (2021). New measurements of long-period radial modes using large earthquakes. *Geophysical Journal International*, 224(2), 1211-1224. <https://doi.org/10.1093/gji/gjaa499>

Widmer, R., Masters, G., & Gilbert, F. (1991). Spherically symmetric attenuation within the Earth from normal mode data. *Geophysical journal international*, 104(3), 541-553. <https://doi.org/10.1111/j.1365-246X.1991.tb05700.x>

Zábranová, E., & Matyska, C. (2017). Low-frequency centroid moment tensor inversion of the 2015 Illapel earthquake from superconducting-gravimeter data. In *The Chile-2015 (Illapel) Earthquake and Tsunami* (pp. 65-71). Birkhäuser, Cham. [https://doi.org/10.1007/978-3-319-57822-4\\_6](https://doi.org/10.1007/978-3-319-57822-4_6)